

RESEARCH ARTICLE

Open Access



Design and structural characterisation of olfactomedin-1 variants as tools for functional studies

Matti F. Pronker^{1,2*} , Hugo van den Hoek^{2,3}  and Bert J. C. Janssen^{2*} 

Abstract

Background: Olfactomedin-1 (Olfm1; also known as Noelin or Pancortin) is a highly-expressed secreted brain and retina protein and its four isoforms have different roles in nervous system development and function. Structural studies showed that the long Olfm1 isoform BMZ forms a disulfide-linked tetramer with a V-shaped architecture. The tips of the Olfm1 “V” each consist of two C-terminal β -propeller domains that enclose a calcium binding site. Functional characterisation of Olfm1 may be aided by new biochemical tools derived from these core structural elements.

Results: Here we present the production, purification and structural analysis of three novel monomeric, dimeric and tetrameric forms of mammalian Olfm1 for functional studies. We characterise these constructs structurally by high-resolution X-ray crystallography and small-angle X-ray scattering. The crystal structure of the Olfm1 β -propeller domain (to 1.25 Å) represents the highest-resolution structure of an olfactomedin family member to date, revealing features such as a hydrophilic tunnel containing water molecules running into the core of the domain where the calcium binding site resides. The shorter Olfactomedin-1 isoform BMY is a disulfide-linked tetramer with a shape similar to the corresponding region in the longer BMZ isoform.

Conclusions: These recombinantly-expressed protein tools should assist future studies, for example of biophysical, electrophysiological or morphological nature, to help elucidate the functions of Olfm1 in the mature mammalian brain. The control over the oligomeric state of Olfm1 provides a firm basis to better understand the role of Olfm1 in the (trans-synaptic) tethering or avidity-mediated clustering of synaptic receptors such as post-synaptic AMPA receptors and pre-synaptic amyloid precursor protein. In addition, the variation in domain composition of these protein tools provides a means to dissect the Olfm1 regions important for receptor binding.

Keywords: Nervous system, Signalling, Synapse, Protein purification, X-ray crystallography, Small-angle X-ray scattering

Background

Olfactomedin family proteins play important roles in nervous system function and development throughout the animal kingdom [1, 2]. The prototypical member Olfm1 is a secreted glycoprotein expressed at high levels in the brain [3, 4]. As a result of alternative promotor usage and

splicing, Olfm1 exists in four isoforms [5], referred to as AMY, BMY, AMZ and BMZ. The letters A, B, M, Y and Z refer to the different exons in each isoform in corresponding sequential order from N- to C-terminus (Fig. 1). These isoforms are differentially expressed in discrete brain regions and over the course of development [5].

The four isoforms share the M exon, which contains a central tetramerisation domain (denoted N-terminal tetramerisation, NTT) [6] that has not been structurally characterised. Otherwise the isoforms differ at the N- and C-termini. The A isoforms have an alternative signal peptide but no unique residues in the mature protein and represent a truncation at the N-terminus of

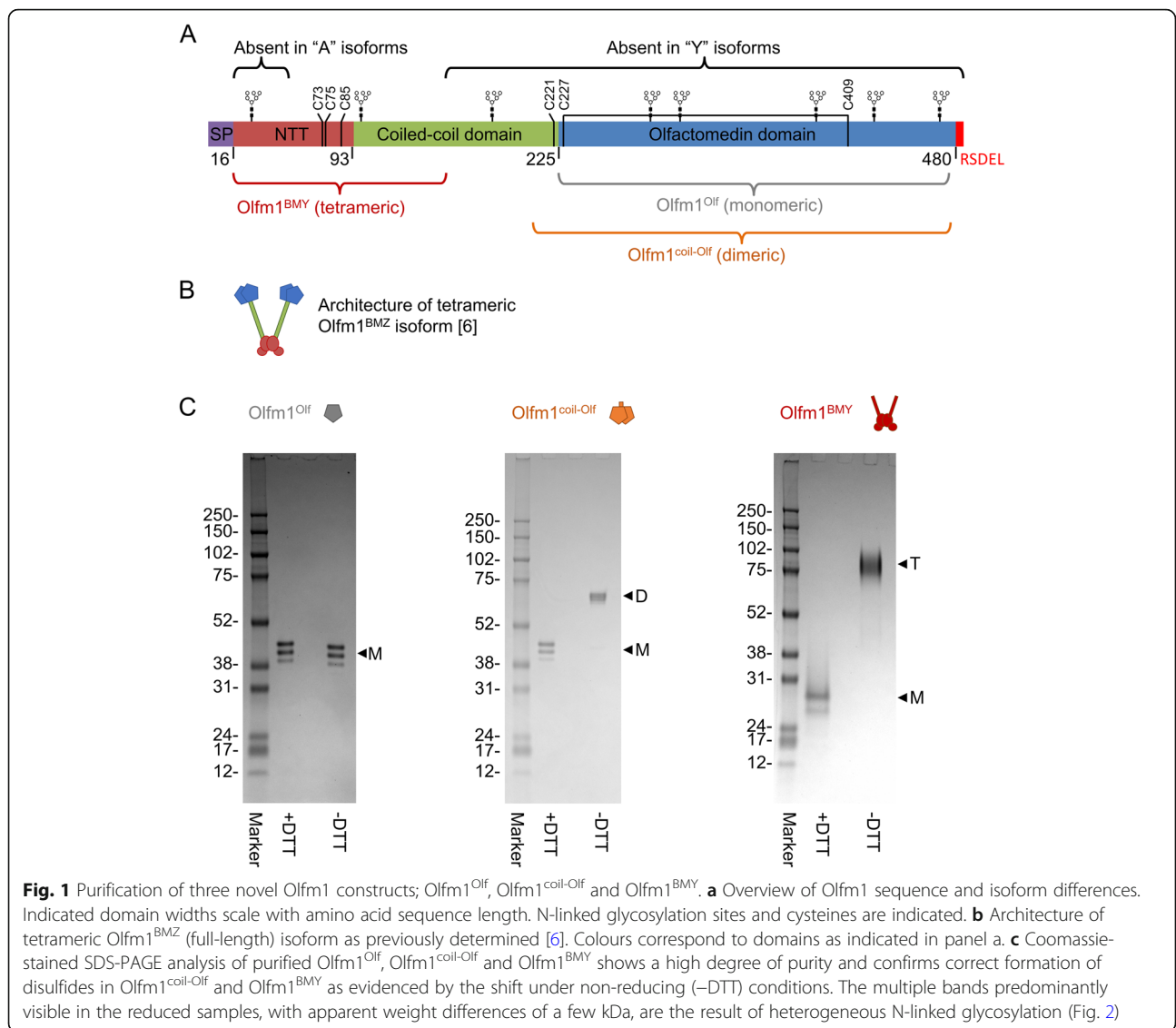
* Correspondence: m.f.pronker@uu.nl; b.j.c.janssen@uu.nl

¹MRC Laboratory of Molecular Biology, Division of Neurobiology, Francis Crick Avenue, Cambridge CB2 0QH, UK

²Bijvoet Center for Biomolecular Research, Utrecht University, Crystal and Structural Chemistry, Kruytgebouw, Padualaan 8, 3584 CH Utrecht, The Netherlands

Full list of author information is available at the end of the article





a contiguous stretch of 34 residues compared to the B isoforms. C-terminal of the NTT is a parallel dimeric coiled-coil segment. Y isoforms end with a single glycine residue (Gly153) at the C-terminus of this coiled coil segment (Fig. 1). The longer Z isoforms on the other hand have a more extended coiled coil (69 residues longer), followed by a highly conserved β-propeller domain (residues 226–478) at the C-terminus that represents more than half the protein mass (Fig. 1). These Z isoforms are substantially more abundant in the brain than the shorter Y isoforms [7, 8]. The β-propellers in the Z isoforms are covalently dimerised by an inter-chain disulfide bond (formed by Cys221-Cys221) at the C-terminus of the preceding coiled-coil domain [6]. It is likely that all four isoforms of Olfm1 form disulfide-linked tetramers by disulfide bonds in the NTT domain that they have in common and that

this tetrameric nature is important for the function of Olfm1, for example by allowing Olfm1 to cluster multiple cell-surface receptors.

Although the exact functions of Olfm1 in the brain are not understood at the mechanistic level, several studies have found roles for Olfm1 in nervous system development of different vertebrates. Olfm1 was found to stimulate neurogenesis [9], play a role in neural crest generation [10] and stimulate axonal elongation [11]. However, expression of Olfm1 still increases strongly from embryonic and juvenile stages into adulthood in mice [7, 12], suggesting Olfm1 additionally functions in the adult brain beyond its developmental roles.

Olfm1 has been reported to interact with various nervous system cell surface receptors such as Amyloid Precursor Protein (APP) [13], the Nogo Receptor [14], and glutamate-gated ion channels of the α-amino-3-

hydroxy-5-methyl-4-isoxazolepropionic acid (AMPA) receptor family GluA1–4 [8, 15–24]. In recent years it was found that *Olfm1* is enriched in synapses [8, 22] and proximity labelling identified its presence in the synaptic cleft [25, 26]. Taken together the findings that *Olfm1* is secreted [4, 9, 10], interacts with synaptic cell surface receptors, is enriched in the synapse and is present in the synaptic cleft suggest that *Olfm1* plays a role in this intercellular substructure.

In line with this hypothesis, a mutation that results in deletion of 52 residues in the coiled coil region of *Olfm1* leads to brain dystrophy, altered interaction with synaptic components and aberrant calcium signalling and behaviour in mice [18], as well as functional deficits of the eye [27]. A full knockout of *Olfm1* in zebrafish showed impaired AMPA receptor trafficking and reduced levels of pre- and post-synaptic proteins such as VAMP-2 and GluA2 [22]. Finally, a recent study showed that *Olfm1* decreases surface mobility of synaptic AMPA receptors [8], directly linking *Olfm1* to controlling synaptic plasticity [28]. However, the exact role and the mechanisms by which *Olfm1* exerts those functions are yet to be determined.

In recent years, structures of the Olf domain of a number of olfactomedin family members have been determined, such as those of gliomedin, myocilin, latrophilin-3 and *Olfm1* itself [6, 29–36]. Although progress has been made towards elucidating the functions of *Olfm1* in the (mature) brain, studies are hampered by a lack of molecular tools to dissect *Olfm1* interactions at the mechanistic level. Here we describe new recombinant *Olfm1* constructs and purification strategies to obtain pure monomeric, dimeric and tetrameric variants of mammalian *Olfm1* that can be used for functional studies. We characterise the structures of these constructs by high-resolution X-ray crystallography and small-angle X-ray scattering (SAXS). The structural data indicate the samples are of high quality and suitable as molecular probes to study *Olfm1* function. Moreover, our structures reveal new insights such as a hydrophilic tunnel containing water molecules running into the hydrophobic core of the C-terminal β -propeller domain, that connects to the sodium and calcium binding sites. We also confirm that, similar to other Olf family members [29–35], the bound Na^+ and Ca^{2+} ions stabilise a surface loop at the top face of the β -propeller. Finally, we show that the shorter BMZ isoform forms disulfide-linked tetramers, consistent with the architecture of the longer BMZ isoform [6].

Materials and methods

Constructs

All constructs were obtained via polymerase chain reaction using *Mus musculus* (mouse) *Olfm1* BMZ isoform

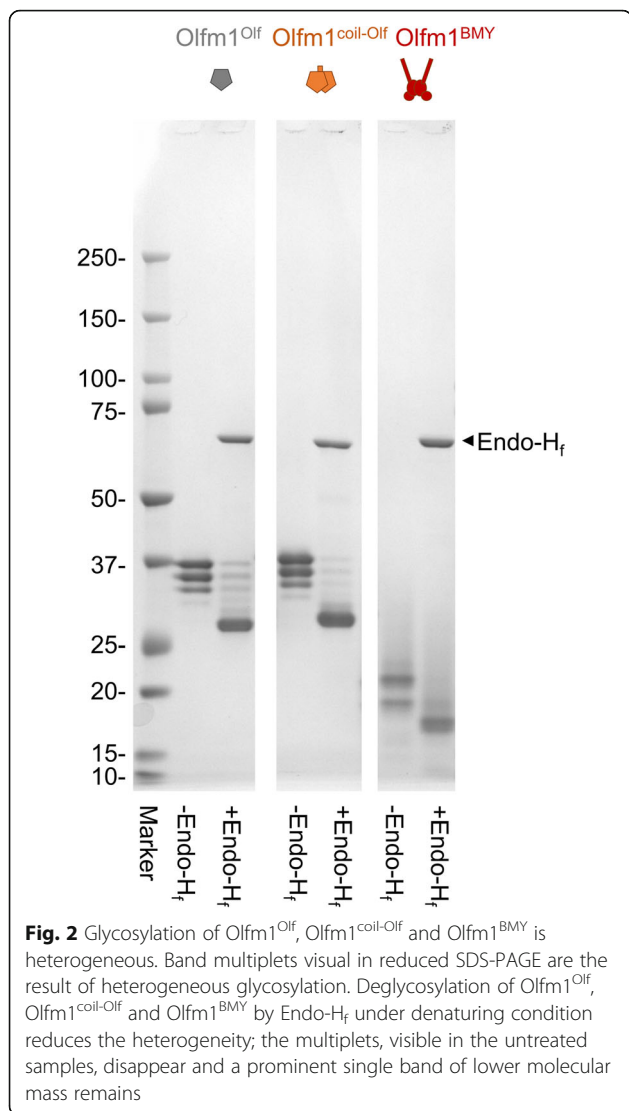
(NCBI Reference Sequence NP_062371) cDNA IRAVp968C0174D (Source Bioscience) as a template. They were subsequently subcloned using BamHI and NotI restriction sites into the pUPE107.03 (U-Protein Express) mammalian expression vector containing an Epstein-Barr virus origin of replication, a C-terminal His₆-tag and a cystatin signal peptide for secretion. Residues (UNIPROT numbering) 226–478 (*Olfm1*^{Olf}), 212–478 (*Olfm1*^{coil-Olf}) or 17–153 (*Olfm1*^{BMZ}; residue 153 being a glycine as in native BMZ), are flanked by an N-terminal GS- and a C-terminal -AAAHHHHHH sequence in the mature protein as a result of the restriction sites and affinity tag. The C-terminal -VIRSEDEL residues have not been included in the *Olfm1*^{Olf} and *Olfm1*^{coil-Olf} constructs as removal enhanced expression and secretion levels.

Protein expression and purification

Constructs were transiently transfected with polyethylenimine in suspension culture growing *N*-acetylglucosaminyltransferase I-deficient (GntI^{-/-}) Epstein-Barr virus nuclear antigen I-expressing HEK293 cells (U-Protein Express) in Freestyle™ medium, following established protocols [37]. After 6 days, cell supernatant was harvested by centrifugation at 1000×g for 15 min and filtered through a 0.22 μm filter. The filtered supernatant was concentrated fivefold and buffer exchanged to 500 mM NaCl, 5 mM CaCl₂, 25 mM HEPES pH 7.8, (IMAC A buffer) using a 10 kDa molecular weight cut-off (MWCO) membrane. Protein was purified by nickel-nitrilotriacetic acid affinity chromatography, using a pre-packed HisTrap column (GE Healthcare). For *Olfm1*^{Olf}, the column was washed with 20 column volumes of IMAC A supplemented with 40 mM imidazole and eluted with IMAC A supplemented with 200 mM imidazole (pH adjusted to pH 7.8 after adding imidazole). Due to their predicted oligomeric nature, washing and elution were performed with higher concentrations of imidazole for *Olfm1*^{coil-Olf} and *Olfm1*^{BMZ}; washing with IMAC A supplemented with 50 mM imidazole (for 20 column volumes) and eluting with 500 mM imidazole in IMAC A.

The eluate was concentrated using 10 kDa MWCO centrifugal filter units (Amicon®). Subsequent purification was performed by size exclusion chromatography (SEC) on a Superdex75 Hiload 16/60 column (for *Olfm1*^{Olf}) or a Superdex200 Hiload 16/60 column (for *Olfm1*^{coil-Olf} and *Olfm1*^{BMZ}) (GE Healthcare), equilibrated in SEC buffer (150 mM NaCl, 2 mM CaCl₂, 20 mM HEPES, pH 7.5). Protein purity, covalent oligomeric state and glycosylation state were assessed by SDS-PAGE (Figs. 1 and 2).

For *Olfm1*^{coil-Olf}, peak fractions containing only disulfide-linked dimer according to non-reducing SDS-PAGE were pooled. Fractions containing disulfide-linked



dimer contaminated with monomer were subjected to a second step of SEC on the same column, allowing more correctly folded disulfide-linked dimer to be recovered (Figs. 1c and 3b). Protein was concentrated to 14.3 mg/mL (Olfm1^{Olf}) or 6 mg/mL (Olfm1^{coil-Olf} and Olfm1^{BM}) using 10 kDa MWCO centrifugal filter units (Amicon®) before aliquoting and plunge-freezing in liquid nitrogen.

Deglycosylation

To test whether the observed heterogeneity (multiplets) on reducing SDS-PAGE (Fig. 1c) was caused by heterogeneous glycosylation, we performed deglycosylation with Endo-H_f (New England Biolabs) under denaturing conditions. Samples were heated to 368 K for 10 min in denaturing buffer (provided with the enzyme) before letting them cool down to 298 K and adding Endo-H_f at a ratio of 1:10 (v/v). The reaction was incubated overnight at 298 K, before performing SDS-PAGE under reducing

conditions together with untreated sample at the same concentration (Fig. 2).

SEC-MALS

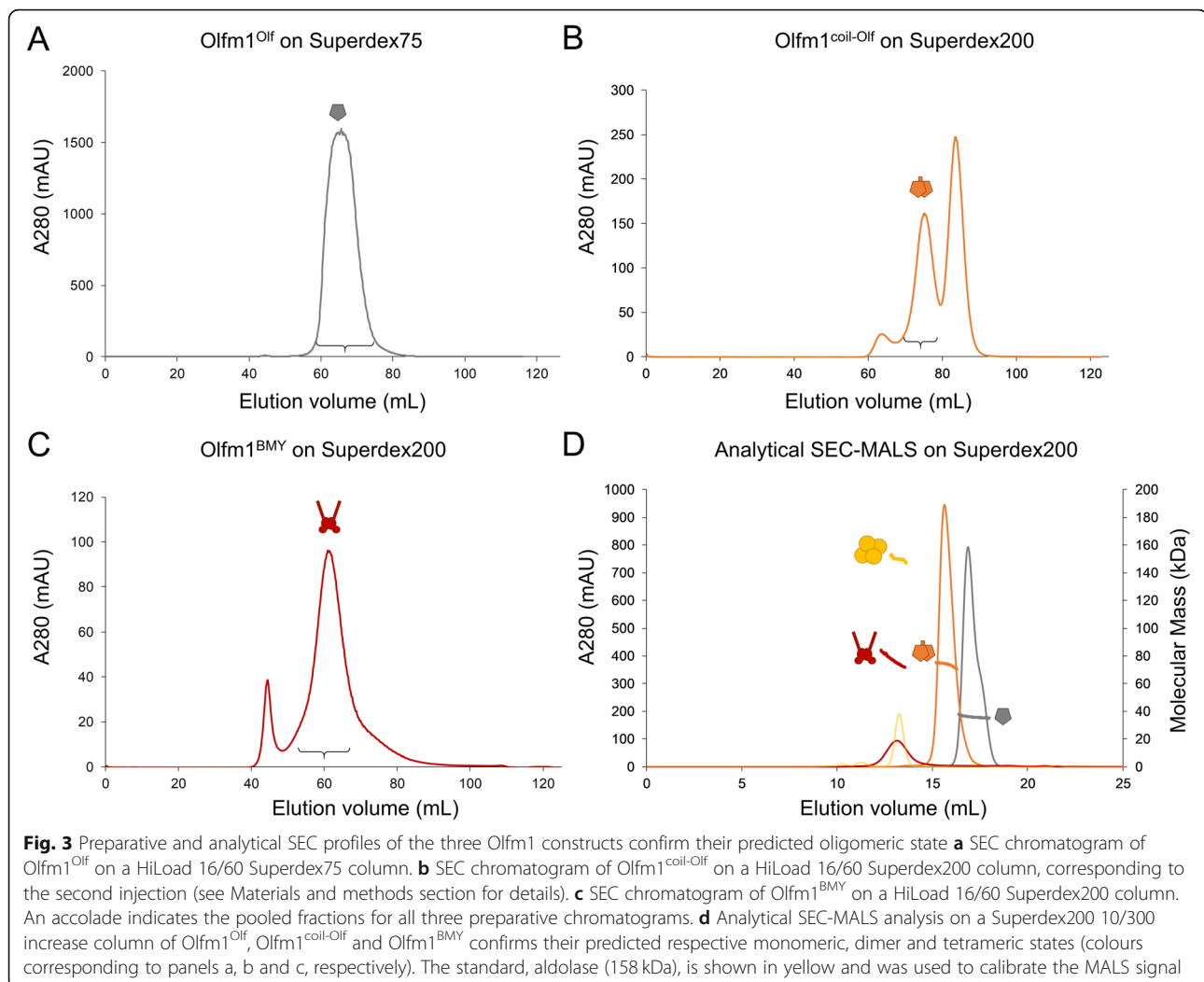
Size-exclusion chromatography with multi-angle light scattering (SEC-MALS) was performed at room temperature using an analytical Superdex200 Increase 10/300 column (GE Healthcare) equilibrated with SEC buffer. SEC was performed with online static light scattering (miniDAWN TREOS, Wyatt Technology) and differential refractive index (dRI, Shimadzu RID-10A) on a Shimadzu HPLC system equipped with a temperature-controlled autosampler (SIL-20 AC, at 277 K) and column oven (CTO-20 AC; at 293 K), at a flowrate of 0.5 mL/min. Data were analysed using the ASTRA software suite (Wyatt Technology). The dRI signal was combined with the light scattering to determine the molecular mass using standard protocols. A dn/dc of 0.178 mL/g was used for Olfm1^{Olf}, and of 0.180 mL/g for Olfm1^{coil-Olf} and Olfm1^{BM}, based on the number of N-linked glycans. Rabbit Aldolase was injected at 1 mg/mL as a control and calibration standard (for Aldolase a dn/dc of 0.186 mL/g was used).

Crystallisation and structure determination

Prior to crystallization, samples of Olfm1^{Olf} and Olfm1^{coil-Olf} were deglycosylated by treatment with Endoglycosidase-H (Endo-H), added at a 1:100 (v/v) ratio and incubating at 37 °C overnight. Crystallization was performed using the sitting drop vapour diffusion method, mixing 150 nL protein sample with 150 nL reservoir solution, at 293 K for Olfm1^{Olf} and at 277 K for Olfm1^{coil-Olf}.

Crystals grew in a condition containing 8% (w/v) PEG 8000 and 0.1 M Tris-HCl pH 8.5 for Olfm1^{Olf} and 0.08 M Magnesium Acetate, 30% (w/v) PEG 4000 and 0.05 M Sodium Cacodylate pH 6.5 for Olfm1^{coil-Olf}. Crystals were cryo-protected with reservoir solution supplemented with 25% (v/v) glycerol before plunge-cooling in liquid nitrogen. Datasets were collected at 100 K at European Synchrotron Radiation Facility (ESRF) beamline ID30A-3 (Massif-3) for Olfm1^{Olf} or Diamond Light Source (DLS) beamline I03 for Olfm1^{coil-Olf}. Grid scanning was used for the Olfm1^{Olf} crystals to find the best-diffracting sub-volume of each crystal.

Data were integrated and scaled by XDS [38] and merged and truncated by the Aimless pipeline [39], respectively. Structures were solved by molecular replacement with PDB 5AMO [6] as a search model using Phaser [40]. Iterative cycles of manual model building in Coot [41] and reciprocal space refinement with Phenix [42] were performed for final refinement. C_α RMSDs were calculated by secondary structure matching using the program superpose [43].



Small-angle X-ray scattering

SAXS was performed at the ESRF BM29 BioSAXS beamline equipped with a 2D Pilatus 1M detector (DECTRIS, Switzerland) operated at an energy of 12.5 keV. Olfm1^{BMY} was diluted with and dialysed against SEC buffer using a 10 kDa MWCO membrane. The concentration of Olfm1^{BMY} was determined by UV spectrophotometry at 280 nm wavelength on a nanodrop ND-1000 spectrophotometer to be 0.615 mg/mL. SAXS data were collected at 277 K. Ten successive 1.0 s frames were collected. The data were radially averaged and normalised to the intensity of the transmitted beam, exposure time, and sample concentration, and the scattering of the solvent blank (SEC buffer) was subtracted. The curve was scaled to absolute values using a water reference so that the I_0 represents the Olfm1 molecular weight. Radiation damage was monitored by comparing curves collected on the same sample; no evidence for radiation damage was observed. Data were analysed by the Atsas suite [44] programs Primus [45] for the Guinier analysis,

Gnom [46] for the pair-distance distribution function and Dammif [47] for the ab-initio modelling.

Results

We produced monomeric, dimeric and tetrameric variants of *Mus musculus* (mouse) Olfm1 in mammalian cells. The monomeric construct comprises the C-terminal Olfactomedin domain (henceforth referred to as Olfm1^{Olf}) (Fig. 1a). The dimeric construct is composed of the Olfactomedin domain and additionally includes part of the coiled coil and the inter-chain disulfide formed by Cys221 at the N-terminus of the Olf domain, similar to our previously crystallised limited proteolysis fragment (Olfm1^{coil-Olf}) [6] (Fig. 1a). The third construct corresponds to the natural isoform BMY (Olfm1^{BMY}) and therefore lacks the C-terminal half of the coiled coil and the Olfactomedin domains (Fig. 1a), but does include the NTT domain and is thus expected to be tetrameric like the full-length BMZ isoform [6].

All constructs were purified from the supernatant of over-expressing HEK293 Gnt1^{-/-} cells by a combination of Ni²⁺-affinity chromatography and SEC (Figs. 1c and 3). Care was taken to always include calcium chloride in the purification buffers as we previously observed this profoundly stabilises full-length Olfm1^{BMZ} [6]. Higher concentrations of imidazole were used for washing and eluting the dimeric Olfm1^{coil-Olf} and tetrameric Olfm1^{BMZ} than for the monomeric Olfm1^{Olf} (see [Materials and methods](#) section for details) as they are expected to have two and four tags per molecule, respectively. We would like to remark that the inclusion of calcium chloride in buffers and the washing and elution with higher concentrations of imidazole (50 instead of 40 mM for washing and 500 instead of 200 mM for elution) also improve the yield and purity of tetrameric Olfm1^{BMZ} (data not shown) compared to our previously-published tetrameric Olfm1^{BMZ} purification strategy [6]. Predicted oligomeric state of the three constructs was confirmed by analytical SEC-MALS (Fig. 3d), revealing molecular masses of 36 ± 1 kDa for Olfm1^{Olf} (35 kDa is predicted for a monomer including 4 N-linked glycans), 73 ± 1 kDa for Olfm1^{coil-Olf} (73 kDa is predicted for a dimer including 8 N-linked glycans) and 77 ± 4 kDa for Olfm1^{BMZ} (77 kDa is predicted for a tetramer including 8 N-linked glycans).

Monomeric Olfm1^{Olf}

Based on our previous structure [6], we designed truncations that are expected to result in a monomeric domain by truncating the dimerizing coiled coil and excluding Cys221 from the construct (Fig. 1, the Olfm1^{Olf} construct includes UNIPROT residues 226–478). This construct expressed with high yields in HEK293 cells (about 30 mg from a litre of HEK293 suspension cell culture) and could be purified using standard protocols (see [Materials and methods](#) section for details).

We determined a high-resolution crystal structure of Endo-H-deglycosylated Olfm1^{Olf} (Fig. 4), which leaves a single acetylglucosamine (GlcNAc) attached to glycosylated asparagines. The deglycosylation step often aids crystallisation. Our best crystal diffracted to 1.25 Å resolution (Table 1), representing the highest resolution crystal structure of an Olfactomedin domain to date. The highly conserved monomeric Olf domain has a five-bladed β -propeller fold with a central metal ion binding site [29–34, 50]. The structure shows a high degree of similarity to the Olf-domain dimer in our previously-determined structure of a dimeric Olfm1^{coil-Olf} (PDB 5AMO) [6] (C_{α} RMSD of 0.55 Å, Fig. 5). A human Olfm1 Olf domain structure derived from bacterially-expressed protein [35] has a very similar structure to our mouse Olfm1^{Olf} (C_{α} RMSD of 0.44 Å, Fig. 6), other than it lacking N-linked glycosylation as a result of the expression system. Comparing the structures of mouse

Olfm1^{Olf} and human Olfm1^{Olf} [35] with that of Olfm1^{coil-Olf}, reveals structural rearrangements arising from the coordination of the Ca²⁺ and Na⁺ ions, that are not present in our previously determined structure of Olfm1^{coil-Olf} [6].

Because of the high resolution of our Olfm1^{Olf} diffraction data to 1.25 Å, we can unambiguously assign a Na⁺ and a Ca²⁺ ion bound in the central cavity of the β -propeller. Metal ion assignment was based on previous binding data [6, 35], coordination distances (Table 2) [51] and fit to the electron density. The Ca²⁺ ion is coordinated by the negatively-charged carboxyl groups of the side chains of Asp356, Asp453 and Glu404, as well as by the backbone carbonyl groups of Ala405 and Leu452 and a single water molecule (Fig. 4b and Table 2 for coordination distances and angles). The Na⁺ ion is also coordinated by the carboxylic acid groups of the side chains of both Asp356 and Asp453, as well as by the backbone carbonyl group of Leu357 and a different water molecule than the one coordinating the calcium ion (Fig. 4b, Table 2). In sum, three formal negative charges of the carboxylic acid groups of the side chains of Asp356, Asp453 and Glu404 are compensated by three formal positive charges of the bound Ca²⁺ and Na⁺ ions.

Two non-bonding interactions appear to be formed between the backbone carbonyl groups of Gly302 and Gln303 with the Na⁺ ion that are at distances too great for direct coordination (2.9 and 3.0 Å, respectively) [52]. Furthermore, several of the coordination angles deviate substantially from 90 ° that may be expected for octahedral metal ion coordination and range from 81.4 to 105.5 ° for the Ca²⁺ ion and from 66.6 to 109.4 ° for the Na⁺ ion (Table 2). Still, the coordination of both Ca²⁺ and Na⁺ ions most closely resembles octahedral geometry (including the two non-bonding interactions with the backbone carbonyls of Gly302 and Gln303), rather than trigonal bipyramid, tetrahedral, square planar or square pyramid. Coordination distances range from 2.3 to 2.4 Å for the Ca²⁺ ion and from 2.2 to 2.4 Å for the Na⁺ ion, excluding the non-bonding interactions with the backbone carbonyls of Gly302 and Gln303. This is close to the ideal distances of 2.3 to 2.4 Å for the Ca²⁺ ion and of 2.3 to 2.5 Å for the Na⁺ ion [51].

A loop connecting propeller blade 2 to blade 3 (residues 339–352, sequence AGYNNMYHYAWGGH) that was unstructured in our previously-determined structure of Olfm1^{coil-Olf} (PDB 5AMO) [6] could now be fully observed in the electron density (Figs. 4 and 5), possibly as a result of a structural transition induced by Na⁺ and Ca²⁺ binding. Because of this structural transition, we will henceforward refer to this loop as the switch loop. The conserved residue Tyr347 stabilises the switch loop by forming a hydrogen bond between the Tyr347

hydroxyl group and the Asp356 carboxyl group (distance 2.7 Å) that plays a central role in coordinating both the bound sodium and calcium ions (Figs. 4 and 5). The Asp356 side chain adopts a different rotamer conformation and is pushed outward in the calcium-free structure [6]. Most likely this outward conformation arises from electrostatic repulsion by the other negatively-charged metal ion coordinating side chains, Glu404 and Asp453, that are no longer compensated by the positive charges of the Ca^{2+} and Na^+ ions in the *apo* form. The outward Asp356 conformation in the *apo* form disrupts the hydrogen bond with Tyr347 and interferes with the conformation of the switch loop as observed in the Ca^{2+} - and Na^+ -bound state by steric hindrance with Tyr347 (Fig. 5), possibly resulting in the switch loop being unstructured in the *apo* form.

The high-resolution crystal structure of Olfm1^{Olf} reveals a hydrophilic tunnel filled with water molecules running from the surface of the Olf domain to the metal ion binding sites (Fig. 4a and c). A similar water-containing tunnel was observed in the structure of the gliomedin Olf domain [29]. In Olfm1, the tunnel starts at the solvent-exposed top face between propeller blade 2 and 3 and runs between these two

blades towards the metal ion binding sites. The tunnel proceeds further, almost to the bottom of the domain where it is closed by a hydrophobic plug made up of residues Pro253 in blade 1, Val359 in blade 3 and Pro456 in blade 5 (Fig. 4a). Twelve ordered water molecules are well resolved in this tunnel due to the high resolution of our electron density map, including the two water molecules involved in coordinating the Na^+ and Ca^{2+} ions. The width of the tunnel varies along the pore axis with radii of 1.0 to 2.2 Å, as determined by the HOLE program [48] (Fig. 4a and c). These tunnel dimensions are too small to allow the passage of hydrated ions. The tunnel may, however, allow dehydrated metal ions, coordinated by tunneling residues, to pass through this pore in the presence of thermal motion at physiological temperatures. Previous work showed that excess calcium stabilises folded purified Olfm1 [6, 35], whereas EDTA (a Ca^{2+} chelator) destabilises it [6]. In addition, sequestering of Ca^{2+} from the propeller domains by the excess of EDTA may increase the flexibility of the switch loop. This implies that calcium ions can dissociate from the folded protein, presumably by diffusion out of the β -propeller domain via the central tunnel.

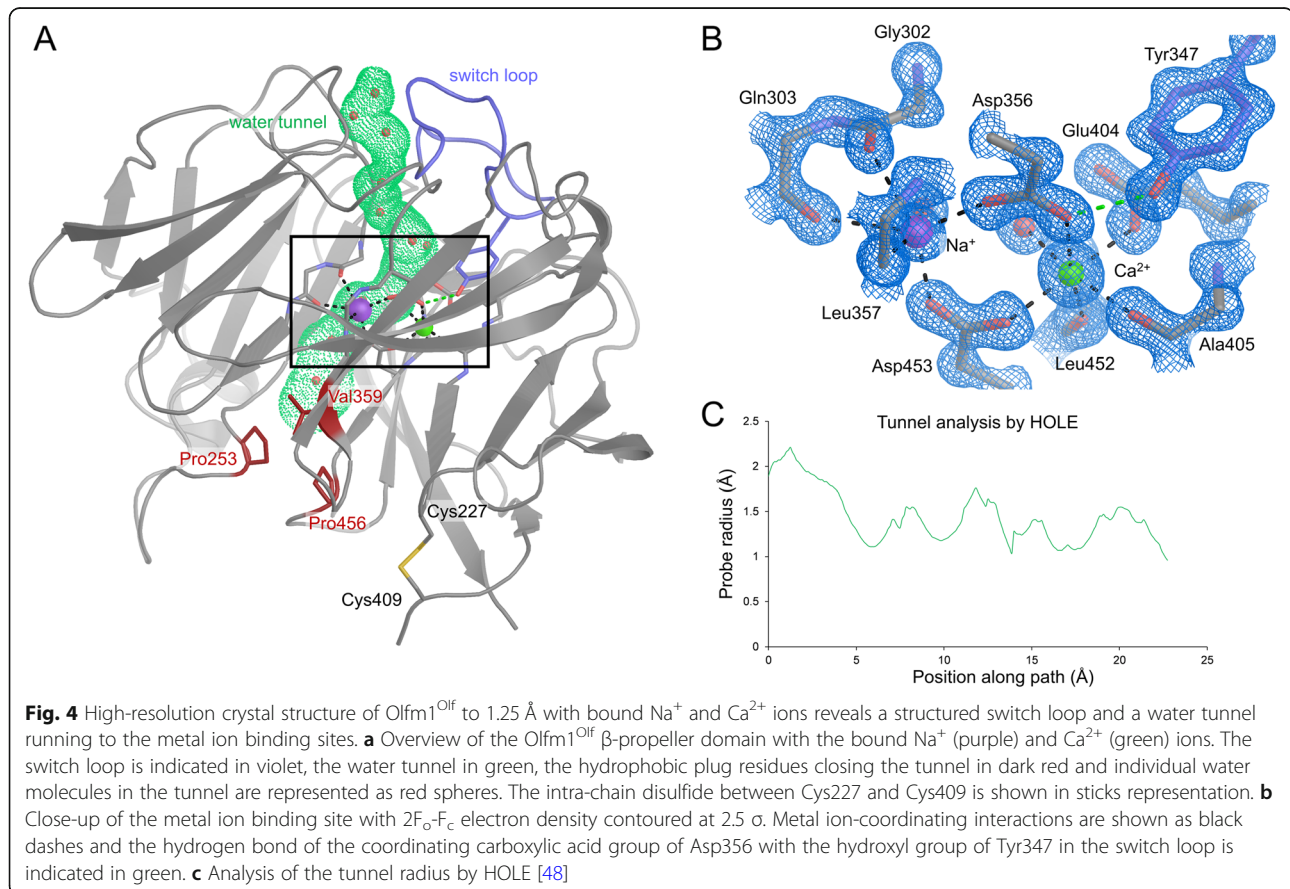


Table 1 Data collection and processing statistics

Data Collection		
PDB ID	6QHJ (Olfm1 ^{Olf})	6QM3 (Olfm1 ^{coil-Olf})
Beamline	ESRF ID30A-3	DLS I03
Resolution range (Å) ^a	36.76–1.25 (1.29–1.25)	75.99–1.89 (2.10–1.89)
Wavelength (Å)	0.9677	0.9762
Space Group	I222	C2
Unit Cell Dimensions		
a, b, c (Å)	61.79, 79.63, 111.72	160.7, 47.0, 105.0
α, β, γ	90.0, 90.0, 90.0	90.0, 117.4, 90.0
Measured reflections	416,910	95,762
Unique reflections	72,028	29,117
Mean I/σ	13.7 (1.0)	10.3 (1.7)
Completeness (%)	94.6 (63.9)	92.2 (77.2)
Redundancy	5.8 (2.4)	3.3 (3.4)
R _{merge} (%)	8.4 (90.8)	6.0 (75.1)
CC _{1/2}	0.998 (0.445)	0.998 (0.551)
Data Refinement		
Resolution Range (Å)	33.75–1.25	71.30–2.00
Total reflections	72,027	28,629
Test set	3623	1459
R _{work}	0.124	0.179
R _{free}	0.141	0.216
No. of protein atoms	4374	4321
No. of ligand atoms	156	133
No. of water atoms	298	99
RMSD from ideal		
Bonds (Å)	0.010	0.007
Angles (°)	1.168	0.852
Mean B factor (Å ²)	17.25	49.09
Ramachandran		
Favoured (%)	96.8	96.4
Outliers (%)	0.4	0.0
Clashscore ^b	1.11	3.58

^aNumbers in parentheses correspond to values for the highest resolution shell

^bValue calculated by MolProbity [49]

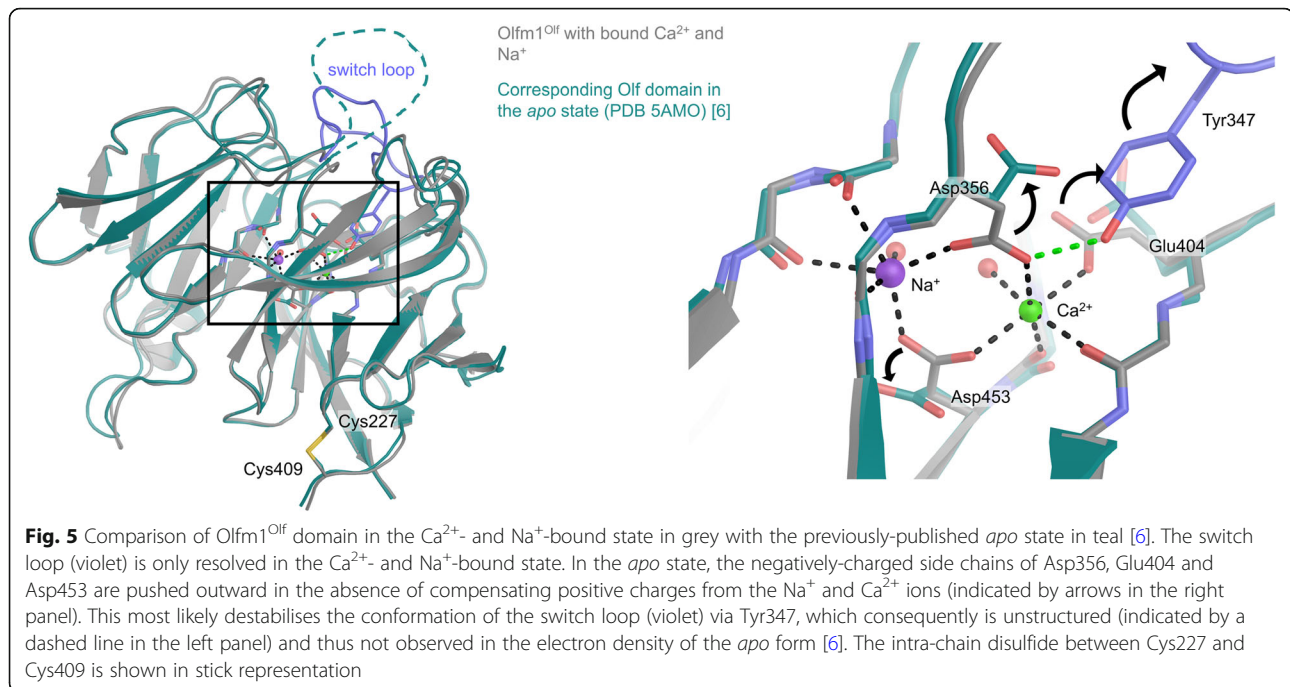
Dimeric Olfm1^{coil-Olf}

A dimeric variant containing part of the coiled coil and Olf domain, corresponding to our previously crystallised proteolysis fragment, was designed with domain boundaries 212–478 (UNIPROT numbering, Fig. 1). This includes Cys221 that forms an inter-chain disulfide and covalently locks this construct in a dimeric form. The better-defined domain boundaries of this construct, compared to our previously described proteolysis fragment [6], provides more control over the quality of this sample. Only about a third of this recombinant Olfm1^{coil-Olf} sample formed disulfide-linked dimers as in the

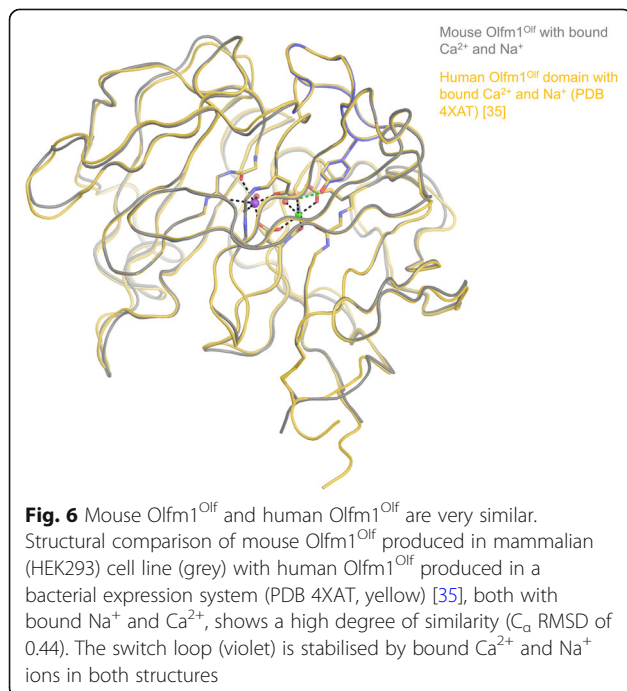
crystal structure, yet the monomeric and dimeric fractions could be separated from each other by two rounds of SEC (Figs. 1c and 3b, see **Materials and methods** section for details). Attempts to rescue the remaining monomeric fraction by reducing the disulfides and refolding in the presence of a redox couple were unsuccessful. The yields of dimeric Olfm1^{coil-Olf} are about 2 mg per litre of suspension HEK293 cell culture.

We crystallised the dimeric form of Olfm1^{coil-Olf}, after deglycosylation with Endo-H, with calcium chloride present in the buffer (Fig. 7a). Olfm1^{coil-Olf} crystallised in the same crystal form (space group C2) as the previously-determined limited proteolysis fragment corresponding to the same segment of Olfm1 (PDB 5AMO) [6], in spite of several differences such as the crystallisation condition, the crystallisation temperature, the presence of bound Ca²⁺ and Na⁺ ions and the glycosylation state. The Olfm1^{coil-Olf} structure reported previously [6] was not deglycosylated indicating that the glycans did not contribute substantially to the crystal packing. The crystals were not fully isomorphous and displayed subtle changes in unit cell parameters. The largest differences are in unit cell dimension b (47.0 Å in this study, whereas 43.9 Å in 5AMO) and angle β (117.4 ° in this study, whereas 114.2 ° in 5AMO). However, apart from the switch loop being observed in the calcium-stabilised conformation similar to the monomeric Olfm1^{Olf} structures discussed above, the structures of the limited proteolysis fragment and recombinantly-expressed Olfm1^{coil-Olf} were highly similar (C_α RMSD of 0.73 Å, Fig. 7b), validating the quality of the sample.

The outward-facing β-propeller top face of the Olf domain has been suggested to be involved in receptor binding [6] because of the conserved nature and the absence of N-linked glycans at this site. The switch loop forms part of this top face in the calcium-bound state and alters the properties of this surface. In the calcium-bound state the top face still consists of conserved residues and is devoid of glycans (Fig. 7c and d, right panel). By altering its conformation upon Ca²⁺ and Na⁺ binding, the switch loop might make this putative interface conditional, i.e. dependent on the presence of Ca²⁺ and/or Na⁺, as has been observed for the olfactomedin family member latrophilin3. Latrophilin3 binds to the cell surface receptor FLRT3 in a calcium-dependent way via the same loop [32]. Another putative region of interaction is the crevice between the two Olf domains, flanked by β-propeller blades 4 and 5 (Fig. 7d). This region is also conserved, void of N-linked glycans and the conformation of the switch loop is not affecting this area. Possibly, the top face of the Olf domains represents a Ca²⁺-dependent conditional interface, whereas the crevice between the two Olf domains is a putative Ca²⁺-independent interface for protein-protein interactions.



The Olfm1 paralogues Olfm2 and Olfm3, which share sequence identity conservation of 56.8–67.5% with Olfm1, have all elements responsible for a similar V-shaped disulfide-linked tetrameric arrangement as observed in Olfm1^{BMZ} (N-terminal cysteines, central coiled-coil domain, C-terminal cysteines and β -propeller domains) [6]. In the β -propeller domain, most of the sequence variation is, as expected, in the surface-exposed



residues. The core of the protein is highly conserved and there are no insertions or deletions in this domain. One notable difference between these three paralogues is the (predicted) N-linked glycosylation pattern (Fig. 7a). Whereas the N-linked glycans on Olfm1 N307 and N473 are conserved in both Olfm2 and Olfm3, the one on N431 is only conserved in Olfm2 but not in Olfm3. The N-linked glycans on N288 and N394 on the other hand are not conserved in either Olfm2 or Olfm3. Other than that, Olfm2 is predicted to have a unique N-linked glycan on its β -propeller domain on N304 (UNIPROT numbering), which corresponds to Olfm1 N342, that is not part of an N-linked glycosylation motif. Olfm1 N342 is surface-exposed and resides in the switch loop. Whether N304 in Olfm2 is actually glycosylated has not been determined. As discussed in detail elsewhere [6, 35], the tertiary structure of the β -propeller domain of Olfm1 is very similar to that of the more distant homologues gliomedin, latrophilin3 and myocilin, yet the switch loop structure and the surface charge distribution of the β -propeller domain differ substantially.

Tetrameric Olfm1^{BMZ}

We expressed a third construct based on the natural shorter BMZ isoform (Olfm1^{BMZ}; UNIPROT residue 17–153, residue 153 being a glycine), that is expected to form disulfide-linked tetramers as it includes the NTT domain. Compared to the longer BMZ isoform, Olfm1^{BMZ} lacks the C-terminal half of the coiled-coil domain as well as the C-terminal Olf domains (Fig. 1). This construct was expressed with reasonable yields (0.5

Table 2 Distances and angles of metal ion coordination in the Olfm1^{Olf} crystal structure

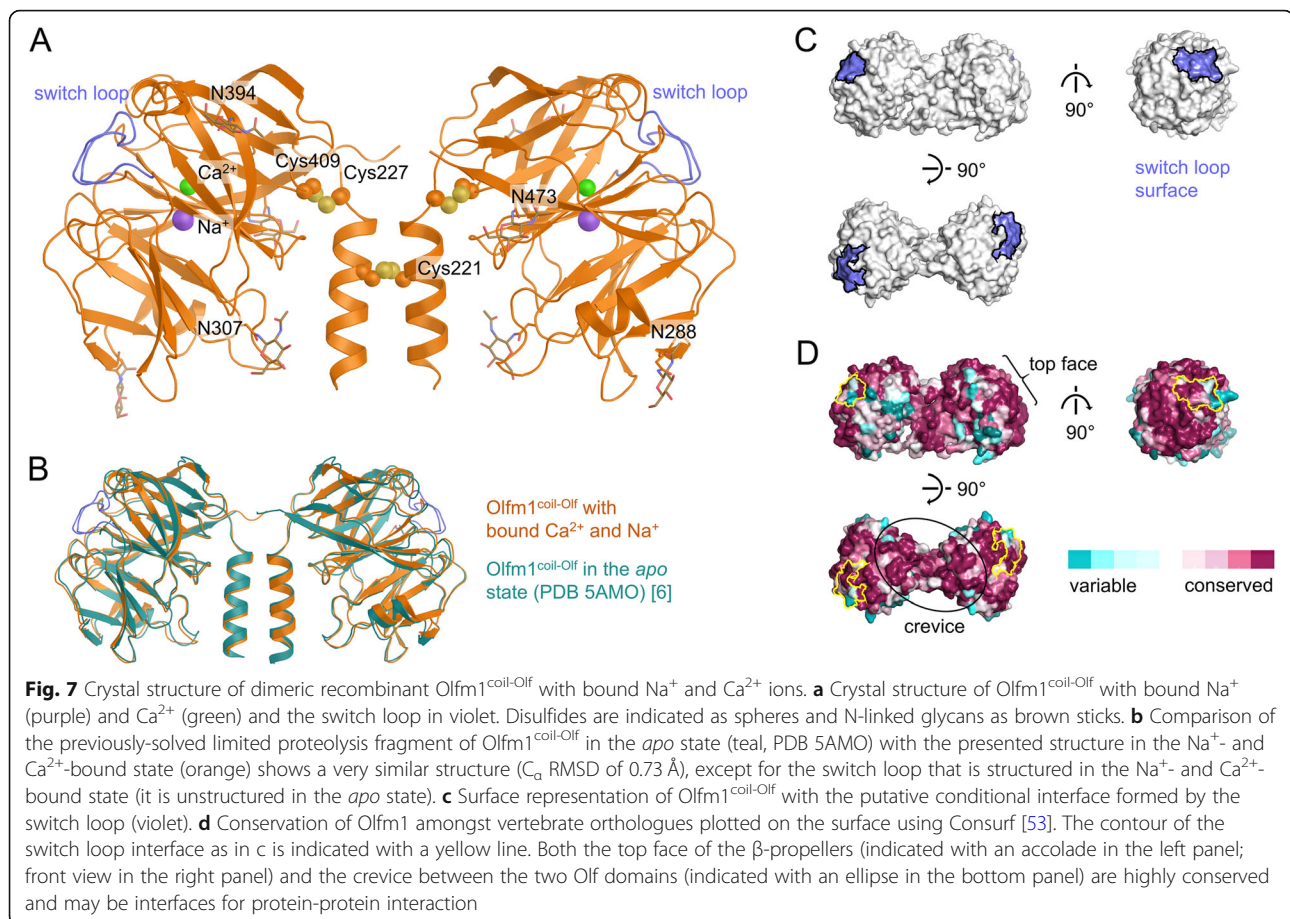
Distances:			Angles:			
		distance (Å)				angle (°)
Calcium	ASP356 O _(carboxylate)	2.3	ASP356 O _(carboxylate)	Calcium	GLU404 O _(carboxylate)	86.7
Calcium	GLU404 O _(carboxylate)	2.3	ASP356 O _(carboxylate)	Calcium	ALA405 O _(carbonyl)	93.1
Calcium	ALA405 O _(carbonyl)	2.3	ASP356 O _(carboxylate)	Calcium	ASP453 O _(carboxylate)	105.5
Calcium	LEU452 O _(carbonyl)	2.3	ASP356 O _(carboxylate)	Calcium	H ₂ O	94.1
Calcium	ASP453 O _(carboxylate)	2.3	GLU404 O _(carboxylate)	Calcium	ALA405 O _(carbonyl)	83.0
Calcium	H ₂ O	2.4	GLU404 O _(carboxylate)	Calcium	LEU452 O _(carbonyl)	83.7
			GLU404 O _(carboxylate)	Calcium	H ₂ O	82.7
Sodium	GLY302 O _(carbonyl)	2.9	ALA405 O _(carbonyl)	Calcium	LEU452 O _(carbonyl)	89.2
Sodium	GLN303 O _(carbonyl)	3.0	ALA405 O _(carbonyl)	Calcium	ASP453 O _(carboxylate)	103.8
Sodium	ASP356 O _(carboxylate)	2.3	LEU452 O _(carbonyl)	Calcium	H ₂ O	81.4
Sodium	LEU357 O _(carbonyl)	2.2	LEU452 O _(carbonyl)	Calcium	ASP453 O _(carboxylate)	83.6
Sodium	ASP453 O _(carboxylate)	2.3	ASP453 O _(carboxylate)	Calcium	H ₂ O	88.4
Sodium	H ₂ O	2.4				
			GLY302 O _(carbonyl)	Sodium	GLN303 O _(carbonyl)	66.6
ASP356 O _(carboxylate)	TYR347 O _(hydroxyl)	2.7	GLY302 O _(carbonyl)	Sodium	ASP356 O _(carboxylate)	88.5
			GLY302 O _(carbonyl)	Sodium	LEU357 O _(carbonyl)	78.3
			GLY302 O _(carbonyl)	Sodium	H ₂ O	98.6
			GLN303 O _(carbonyl)	Sodium	LEU357 O _(carbonyl)	88.4
			GLN303 O (carbonyl)	Sodium	ASP453 O _(carboxylate)	95.8
			GLN303 O (carbonyl)	Sodium	H ₂ O	71.0
			ASP356 O _(carboxylate)	Sodium	LEU357 O _(carbonyl)	101.4
			ASP356 O _(carboxylate)	Sodium	ASP453 O _(carboxylate)	109.4
			ASP356 O _(carboxylate)	Sodium	H ₂ O	99.9
			LEU357 O _(carbonyl)	Sodium	ASP453 O _(carboxylate)	98.5
			ASP453 O _(carboxylate)	Sodium	H ₂ O	77.8

mg per litre of suspension HEK293 cell culture), albeit lower than the Olfm1^{Olf} or Olfm1^{coil-Olf} constructs. The non-reducing gel and SEC-MALS analysis support our prediction that this construct forms a disulfide-linked tetramer (Figs. 1c and 3d). Interestingly, while the light scattering by Olfm1^{BMV} clearly shows it to be tetrameric (determined mass of 76.8 ± 3.6 kDa from the MALS signal; expected 76.8 kDa for a tetramer), the elution volume corresponds to a much larger globular protein (eluting at the same volume as the calibration standard Aldolase; 158 kDa), suggesting Olfm1^{BMV} has an extended conformation. The observation that the tetrameric Olfm1^{BMV} constructs runs as a tetramer on non-reducing gel indicates that the three sets of cysteines in the NTT domain (Cys73, Cys75 and Cys85; Fig. 1a), which could form six disulfide bridges per tetramer, form interchain disulfides across the different sets of chains.

We did not succeed in obtaining crystals of Olfm1^{BMV}, possibly due to the flexible nature of this protein

segment. Therefore, we analysed the structure of Olfm1^{BMV} by SAXS, which provides structural information for proteins in the solution state. The SAXS I_0 suggests a molecular mass of 84.0 kDa for Olfm1^{BMV} (Fig. 8, Table 3). This further supports Olfm1^{BMV} forming tetramers, although the value is higher than the theoretical mass confirmed by SEC-MALS of 76.8 kDa for a tetramer of Olfm1^{BMV} including 2 predicted N-linked glycans per chain. Guinier analysis of the SAXS data shows that Olfm1^{BMV} has a radius of gyration (R_g) of 5.4 nm (Fig. 8b). The pair-distance distribution function $P(r)$ has an asymmetric bell shape with a maximum at 4.76 nm, representing the most commonly occurring inter-atomic distance in the particle (Fig. 8d). The $P(r)$ further shows Olfm1^{BMV} has a maximum dimension D_{max} of 16.3 nm and a Porod volume of 248 nm³. The Kratky plot indicates substantial flexibility, yet still more structure than a random coil (Fig. 8c).

Based on our previous work on the longer BMZ isoform of Olfm1 [6], we expected the Olfm1^{BMV} construct

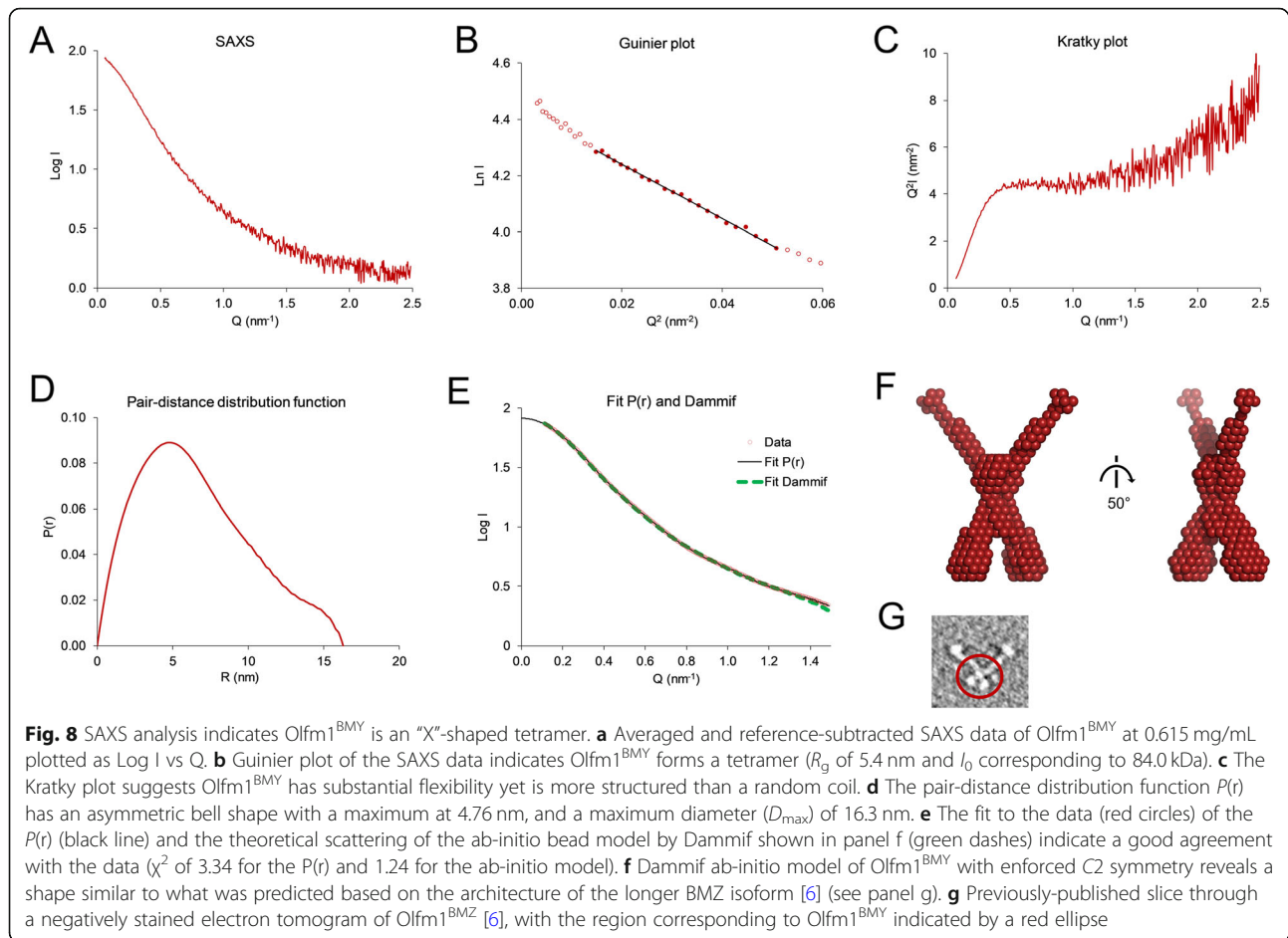


(that makes up the N-terminal part of the longer BMZ isoform) to have two-fold rotational symmetry (C_2). Ab-initio modelling based on our SAXS data using the Dammif software [47] with enforced C_2 symmetry yields models that closely mimic the shape of the Olfm1^{BMZ} N-terminal segment observed previously by negative stain electron tomography (Fig. 8f and g) [6]. Thus, the shift on non-reducing gel, the SEC-MALS analysis and the SAXS data support the notion that this natural isoform folds into tetramers with the same structure as the corresponding region within the longer BMZ isoform.

Discussion

The obtained high-resolution crystal structures of the monomeric Olfm1^{Olf} and dimeric Olfm1^{coil-Olf} constructs in the calcium- and sodium-bound states yield several new insights. Similar to latrophilin [32], a surface loop of Olfactomedin-1 is stabilised by the internally-bound Ca²⁺ and Na⁺ ions in the core of the Olf domain. Ca²⁺ and Na⁺ ions would be able to bind the buried binding sites in the Olf domain during folding in the high calcium environment of the secretory pathway, also in the absence of any tunnel. The presence of this tunnel suggests these metal ion binding sites do not just serve a

structural function. Rather, this tunnel might allow the Olf domain to sample the concentration of these ions in the microenvironment of Olfm1 beyond the ER. The Olf domain of Olfm1 could serve as a calcium sensor by providing a conditional interface for protein-protein interactions, the condition being the presence of Ca²⁺ at sufficiently high concentration. Since Olfm1 was found to be enriched in synapses and present in the synaptic cleft, it is tempting to speculate that synaptic activity, which causes substantial local decreases in extracellular calcium concentration [54] as a result of the opening of pre-synaptic voltage-gated calcium channels and post-synaptic NMDA receptors and calcium-permeable AMPA receptors, might be sampled by the Olf domains of Olfm1. The ability of the Olf domain to sample calcium concentration might serve to control short-term or long-term depression at synapses or prevent excitotoxicity as a negative feedback sensor. Further studies are required to determine if the equilibrium and kinetic dissociation constants (K_d and k_d) for calcium binding are in the correct concentration and time regime to sample such physiological decreases in calcium concentration, and to elucidate what (if any) protein binding partners of Olfm1 are calcium-dependent. Interestingly,



various trans-synaptic protein complexes have been shown to be depending on or stabilised by calcium ions, such as β -Neurexin-neuroligin [55, 56], β -Neurexin-LRRTM2 [57, 58], β -Neurexin-Cerebellin1-GluD2 [59], Cadherins [60, 61], and Latrophilin3-Flrt [32], suggesting this might be a more general mechanism.

In this regard, another attractive hypothesis that could be studied with our constructs would be that Olfm1 is involved in trans-synaptic interactions. Olfm1 binds directly to post-synaptic AMPA receptors [8] and has a V-shaped oligomeric architecture similar to the secreted protein Cerebellin1 [6, 59], which engages with the AMPA receptor homologue GluD2 in the synaptic cleft of specific synapses [59, 62, 63]. Cerebellin1 tethers

these GluD2 receptors to pre-synaptic β -Neurexin [59, 63]. AMPA receptors were recently found to be aligned on a subsynaptic scale to pre-synaptic vesicle release sites [64]. The similar architecture of Olfm1 and Cerebellin1 suggests Olfm1 might bind to AMPA receptors in a similar manner as Cerebellin1 to GluD2 receptors.

A putative pre-synaptic anchor for Olfm1 (analogous to β -Neurexin for Cerebellin-1) could be APP, a single-pass transmembrane protein that is known to be associated with the pre-synaptic vesicle release machinery [65, 66]. APP was found previously to interact directly with Olfm1, thereby modulating the proteolytic processing of APP by secretase enzymes [13]. The tetrameric nature, shape and dimensions of Olfm1^{BMZY} might allow it to engage multiple pre- and post-synaptic receptors, benefitting from surface avidity similar to for example IgGs [67]. Further research is required to determine if Olfm1 can simultaneously engage both pre-synaptic APP and post-synaptic AMPA receptors. If Olfm1 does trans-synaptically tether AMPA receptors to APP in vivo, this could potentially have implications for Alzheimer’s disease, as mutations affecting the proteolytic processing of APP (both in

Table 3 SAXS parameters of Olfm1^{BMZY}

SASBDB code	SASDF96
Concentration (mg/mL)	0.615
R_g (nm)	5.4
l_0	84.0
D_{max} (nm)	16.3
Porod Volume (nm ³)	248

APP itself and its secretases) are well-known to cause early-onset Alzheimer's disease [68, 69], the early phase of which is characterised by a loss of AMPA receptors and synaptic malfunctioning [70–72].

Conclusions

Here we present three novel constructs of Olfm1; one monomeric (Olfm1^{Olf}), one dimeric (Olfm1^{coil-Olf}) and one tetrameric (Olfm1^{BMZ}), with optimised expression and purification strategies. We validated our expression and purification strategies by analysing the samples by (non)-reducing SDS-PAGE and analytical SEC-MALS. Furthermore, we determined high-resolution crystal structures for the monomeric and dimeric constructs, and characterised the size and shape of the tetrameric Olfm1^{BMZ} construct by SAXS. These constructs, in combination with our previously-published tetrameric BMZ construct [6], will allow the precise probing of interactions of binding partners with specific domains of Olfm1, and can be used in functional assays to study Olfm1 in the (mature) mammalian brain.

The constructs and purification strategies presented here could be used to find domain-specific and calcium-dependent binding partners. For example, the protein samples could be used as probes to identify novel Olfm1 interactors by proteomic screening of interaction partners pulled down by Olfm1-functionalised beads from brain lysate in the presence of either calcium or EDTA. Both new and established interactions could be further quantified and assigned to specific domains by direct binding assays such as surface plasmon resonance and isothermal titration calorimetry with the described constructs. These new constructs, together with our previously published tetrameric Olfm1^{BMZ} construct, could also be used for *in vitro* cell or bead clustering assays to test if pre/post-synaptic receptor binding *in trans* is supported by Olfm1. Moreover, the Olfm1^{BMZ} and Olfm1^{coil-Olf} constructs could be used as acute dominant negatives by interfering with one interaction but not linking to a third protein in functional assays, such as electrophysiological determination of synaptic input/output ratio or long-term potentiation, or morphological characterisation of synapses and dendritic spines, for example in combination with knockout or knockdown animals [22]. In conclusion, there are many exciting hypotheses about the functions of Olfm1 in the mature (mammalian) brain that remain to be tested, for which our novel constructs and their associated purification strategies might provide a starting point.

Abbreviations

AMPA: α -amino-3-hydroxy-5-methyl-4-isoxazolepropionic acid; APP: Amyloid precursor protein; DLS: Diamond light source; ESRF: European Synchrotron Radiation Facility; Gnt1: *N*-acetylglucosaminyltransferase I; MWCO: Molecular weight cut-off; NMDA: *N*-Methyl-D-aspartic acid; NTT: N-terminal

tetramerisation domain; Olf: Olfactomedin; RMSD: Root mean square deviation; SAXS: Small-angle X-ray scattering

Acknowledgements

The SAXS experiments on Olfm1^{BMZ} were performed on the BM29 beamline and the diffraction experiments for Olfm1^{Olf} were performed on the ID30A-3 beamline, both at the ESRF, Grenoble, France. The diffraction experiments for Olfm1^{coil-Olf} were performed at I03 at DLS, Harwell, United Kingdom. We are grateful to local contacts at the ESRF and DLS for assistance in using beamlines BM29, ID30A-3 and I03. We thank Dr. Mercedes Ramírez Escudero for assistance with protein purification and Matthieu Zeronian for assistance with SEC-MALS experiments.

Authors' contributions

HvdH designed constructs and tested expression in small scale. MFP and HvdH expressed constructs in large scale and optimised purification. MFP performed X-ray crystallography, SEC-MALS and SAXS experiments, and analysed the data. MFP and BJCJ supervised the project. MFP and BJCJ wrote the manuscript with input from HvdH. All authors read and approved the final manuscript.

Funding

This work was supported by Netherlands Organisation for Scientific Research (NWO) VIDI Grant 723.012.002. B.J.C.J. is supported by a European Research Council Starting Grant (677500).

Availability of data and materials

The atomic coordinates and structure factors (codes 6QHJ and 6QM3 for Olfm1^{Olf} and Olfm1^{coil-Olf}, respectively) have been deposited in the Protein Data Bank (<http://www.pdb.org/>). The SAXS data and models of Olfm1^{BMZ} have been deposited in the small angle scattering databank (<https://www.sasbdb.org/>) with accession code SASDF96.

Ethics approval and consent to participate

Not applicable

Consent for publication

Not applicable

Competing interests

The authors declare that they have no competing interests.

Author details

¹MRC Laboratory of Molecular Biology, Division of Neurobiology, Francis Crick Avenue, Cambridge CB2 0QH, UK. ²Bijvoet Center for Biomolecular Research, Utrecht University, Crystal and Structural Chemistry, Kruytgebouw, Padualaan 8, 3584 CH Utrecht, The Netherlands. ³Department of Molecular Structural Biology, Max Planck Institute for Biochemistry, Am Klopferspitz 18, 82152 Martinsried, Germany.

Received: 29 May 2019 Accepted: 10 October 2019

Published online: 14 November 2019

References

- Anholt RRH. Olfactomedin proteins: central players in development and disease. *Front Cell Dev Biol.* 2014;2:1–10. <https://doi.org/10.3389/fcell.2014.00006>.
- Li Q, Liu A, Gu X, Su Z. Olfactomedin domain-containing proteins: evolution, functional divergence, expression patterns and damaging SNPs. *Mol Gen Genomics.* 2019. <https://doi.org/10.1007/s00438-019-01549-9>.
- Chen PB, Kawaguchi R, Blum C, Achiro JM, Coppola G, O'Dell TJ, et al. Mapping gene expression in excitatory neurons during hippocampal late-phase long-term potentiation. *Front Mol Neurosci.* 2017;10:1–16. <https://doi.org/10.3389/fnmol.2017.00039>.
- Begcevic I, Brinc D, Drabovich AP, Batruch I, Diamandis EP. Identification of brain-enriched proteins in the cerebrospinal fluid proteome by LC-MS/MS profiling and mining of the human protein atlas. *Clin Proteomics.* 2016;13:1–13.
- Danielson PE, Forss-Petter S, Battenberg ELF, de Lecea L, Bloom FE, Sutcliffe JG. Four structurally distinct neuron-specific olfactomedin-related

- glycoproteins produced by differential promoter utilization and alternative mRNA splicing from a single gene. *J Neurosci Res.* 1994;38:468–78.
6. Pronker MF, Bos TGAA, Sharp TH, Thies-Weesie DME, Janssen BJC. Olfactomedin-1 Has a V-shaped disulfide-linked tetrameric structure. *J Biol Chem.* 2015;290:15092–101 <http://www.jbc.org/lookup/doi/10.1074/jbc.M115.653485>.
 7. Cheng A, Arumugam TV, Liu D, Khatri RG, Mustafa K, Kwak S, et al. Pancortin-2 interacts with WAVE1 and Bcl-xL in a mitochondria-associated protein complex that mediates ischemic neuronal death. *J Neurosci.* 2007;27:1519–28.
 8. Pandya NJ, Seeger C, Babai N, Gonzalez-Lozano MA, Mack V, Lodder JC, et al. Noelin1 affects lateral mobility of synaptic AMPA receptors. *Cell Rep.* 2018;24:1218–30. <https://doi.org/10.1016/j.celrep.2018.06.102>.
 9. Moreno T a, Bronner-Fraser M. The secreted glycoprotein Noelin-1 promotes neurogenesis in *Xenopus*. *Dev Biol.* 2001;240:340–60.
 10. Barembaum M, Moreno T a, La Bonne C, Sechrist J, Bronner-Fraser M. Noelin-1 is a secreted glycoprotein involved in generation of the neural crest. *Nat Cell Biol.* 2000;2:219–25.
 11. Nakaya N, Lee H-S, Takada Y, Tzchori I, Tomarev SI. Zebrafish olfactomedin 1 regulates retinal axon elongation in vivo and is a modulator of Wnt signaling pathway. *J Neurosci.* 2008;28:7900–10.
 12. Gonzalez-Lozano MA, Klemmer P, Gebuis T, Hassan C, van Nierop P, van Kesteren RE, et al. Dynamics of the mouse brain cortical synaptic proteome during postnatal brain development. *Sci Rep.* 2016;6:35456. <https://doi.org/10.1038/srep35456>.
 13. Rice HC, Townsend M, Bai J, Suth S, Cavanaugh W, Selkoe DJ, et al. Pancortins interact with amyloid precursor protein and modulate cortical cell migration. *Development.* 2012;139:3986–96.
 14. Nakaya N, Sultana A, Lee HS, Tomarev SI. Olfactomedin 1 interacts with the Nogo A receptor complex to regulate axon growth. *J Biol Chem.* 2012;287:37171–84.
 15. von Engelhardt J, Mack V, Sprengel R, Kavenstock N, Li KW, Stern-Bach Y, et al. CKAMP44: a brain-specific protein attenuating short-term synaptic plasticity in the dentate gyrus. *Science.* 2010;327:1518–22. <https://doi.org/10.1126/science.1184178>.
 16. Shanks NF, Savas JN, Maruo T, Cais O, Hirao A, Oe S, et al. Differences in AMPA and Kainate receptor interactomes facilitate identification of AMPA receptor auxiliary subunit GSG1L. *Cell Rep.* 2012;1:590–8. <https://doi.org/10.1016/j.celrep.2012.05.004>.
 17. Schwenk J, Harmel N, Brechet A, Zolles G, Berkefeld H, Müller CS, et al. High-resolution proteomics unravel architecture and molecular diversity of native AMPA receptor complexes. *Neuron.* 2012;74:621–33.
 18. Nakaya N, Sultana A, Munasinghe J, Cheng A, Mattson MP, Tomarev SI. Deletion in the N-terminal half of olfactomedin 1 modifies its interaction with synaptic proteins and causes brain dystrophy and abnormal behavior in mice. *Exp Neurol.* 2013;250:205–18.
 19. Sultana A, Nakaya N, Dong L, Abu-Asab M, Qian H, Tomarev SI. Deletion of olfactomedin 2 induces changes in the AMPA receptor complex and impairs visual, olfactory, and motor functions in mice. *Exp Neurol.* 2014;261:802–11. <https://doi.org/10.1016/j.expneurol.2014.09.002>.
 20. Chen N, Pandya NJ, Koopmans F, Castelo-Székely V, van der Schors RC, Smit AB, et al. Interaction proteomics reveals brain region-specific AMPA receptor complexes. *J Proteome Res.* 2014;13:5695–706. <https://doi.org/10.1021/pr500697b>.
 21. Schwenk J, Baehrens D, Haupt A, Bildl W, Boudkzazi S, Roepner J, et al. Regional diversity and developmental dynamics of the AMPA-receptor proteome in the mammalian brain. *Neuron.* 2014;84:41–54. <https://doi.org/10.1016/j.neuron.2014.08.044>.
 22. Nakaya N, Sultana A, Tomarev SI. Impaired AMPA receptor trafficking by a double knockout of zebrafish olfactomedin1a/b. *J Neurochem.* 2017;143:635–44.
 23. Brechet A, Buchert R, Schwenk J, Boudkzazi S, Zolles G, Siquier-Pernet K, et al. AMPA-receptor specific biogenesis complexes control synaptic transmission and intellectual ability. *Nat Commun.* 2017;8:15910.
 24. Schmitz LJM, Klaassen RV, Ruiperez-Alonso M, Zamri AE, Stroeder J, Rao-Ruiz P, et al. The AMPA receptor-associated protein Shisa7 regulates hippocampal synaptic function and contextual memory. *Elife.* 2017;6:1–28.
 25. Loh KH, Stawski PS, Draycott AS, Udeshi ND, Lehrman EK, Wilton DK, et al. Proteomic analysis of unbounded cellular compartments: synaptic clefts. *Cell.* 2016;166:1295–1307.e21. <https://doi.org/10.1016/j.cell.2016.07.041>.
 26. Cijssouw T, Ramsey A, Lam T, Carbone B, Blanpied T, Biederer T, et al. Mapping the proteome of the synaptic cleft through proximity labeling reveals new cleft proteins. *Proteomes.* 2018;6:48. <https://doi.org/10.3390/proteomes6040048>.
 27. Koch MA, Rosenhammer B, Paper W, Volz C, Braunger BM, Hausberger J, et al. Mutated olfactomedin 1 in the interphotoreceptor matrix of the mouse retina causes functional deficits and vulnerability to light damage. *Histochem Cell Biol.* 2017;147:453–69.
 28. Penn AC, Zhang CL, Georges F, Royer L, Breillat C, Hosy E, et al. Hippocampal LTP and contextual learning require surface diffusion of AMPA receptors. *Nature.* 2017;549:384–8. <https://doi.org/10.1038/nature23658>.
 29. Han H, Kursula P. The olfactomedin domain from gliomedin is a β -propeller with unique structural properties. *J Biol Chem.* 2015;290:3612–21 <http://www.jbc.org/lookup/doi/10.1074/jbc.M114.627547>.
 30. Donegan RK, Hill SE, Freeman DM, Nguyen E, Orwig SD, Turnage KC, et al. Structural basis for misfolding in myocilin-associated glaucoma. *Hum Mol Genet.* 2015;24:2111–24 <http://www.hmg.oxfordjournals.org/cgi/doi/10.1093/hmg/ddu730>.
 31. Jackson VA, del Toro D, Carrasquero M, Roversi P, Harlos K, Klein R, et al. Structural basis of latrophilin-FLRT interaction. *Structure.* 2015;23(4):774–81. <http://linkinghub.elsevier.com/retrieve/pii/S0969212615000374>.
 32. Ranaivoson FM, Liu Q, Martini F, Bergami F, von Daake S, Li S, et al. Structural and mechanistic insights into the latrophilin3-FLRT3 complex that mediates glutamatergic synapse development. *Structure.* 2015;23:1665–77. <https://doi.org/10.1016/j.str.2015.06.022>.
 33. Lu YC, Nazarko OV, Sando R, Salzman GS, Südhof TC, Araç D. Structural basis of latrophilin-FLRT-UNC5 interaction in cell adhesion. *Structure.* 2015;23:1678–91.
 34. Jackson VA, Mehmood S, Chavent M, Roversi P, Carrasquero M, Del Toro D, et al. Super-complexes of adhesion GPCRs and neural guidance receptors. *Nat Commun.* 2016;7:11184. <https://doi.org/10.1038/ncomms11184>.
 35. Hill SE, Donegan RK, Nguyen E, Desai TM, Lieberman RL. Molecular details of olfactomedin domains provide pathway to structure-function studies. *PLoS One.* 2015;10:e0130888. <https://doi.org/10.1371/journal.pone.0130888>.
 36. Patterson-orazem AC, Hill SE, Wang Y, Dominic IM, Hall CK, Lieberman RL. Differential misfolding properties of glaucoma-associated olfactomedin domains from human and mouse department of chemical & biomolecular engineering, North Carolina State University. *Biochemistry.* 2019;58:1718.
 37. Geisse S, Henke M. Large-scale transient transfection of mammalian cells: a newly emerging attractive option for recombinant protein production. *J Struct Funct Genom.* 2005;6:165–70.
 38. Kabsch W. Xds. *Acta Crystallogr Sect D Biol Crystallogr.* 2010;66:125–32.
 39. Evans PR, Murshudov GN. How good are my data and what is the resolution? *Acta Crystallogr Sect D Biol Crystallogr.* 2013;69:1204–14.
 40. McCoy AJ, Grosse-Kunstleve RW, Adams PD, Winn MD, Storoni LC, Read RJ. Phaser crystallographic software. *J Appl Crystallogr.* 2007;40:658–74.
 41. Emsley P, Cowtan K. Coot: model-building tools for molecular graphics. *Acta Crystallogr Sect D Biol Crystallogr.* 2004;60:2126–32.
 42. Afonine PV, Grosse-Kunstleve RW, Echols N, Headd JJ, Moriarty NW, Mustyakimov M, et al. Towards automated crystallographic structure refinement with phenix.refine. *Acta Crystallogr Sect D Biol Crystallogr.* 2012;68:352–67.
 43. Krissinel E, Henrick K. Secondary-structure matching (SSM), a new tool for fast protein structure alignment in three dimensions research papers. *Acta Crystallogr Sect D Biol Crystallogr.* 2004;60:2256–68.
 44. Petoukhov MV, Franke D, Shkumatov AV, Tria G, Kikhney AG, Gajda M, et al. New developments in the ATSAS program package for small-angle scattering data analysis. *J Appl Crystallogr.* 2012;45:342–50.
 45. Konarev PV, Volkov WV, Sokolova AV, Koch MHJ, Svergun DI. PRIMUS: a windows PC-based system for small-angle scattering data analysis. *J Appl Crystallogr.* 2003;36:1277–82.
 46. Svergun DI. Determination of the regularization parameter in indirect-transform methods using perceptual criteria. *J Appl Crystallogr.* 1992;25:495–503.
 47. Franke D, Svergun DI. DAMMIF, a program for rapid ab-initio shape determination in small-angle scattering. *J Appl Crystallogr.* 2009;42:342–6.
 48. Smart OS, Neduevelil JG, Wang X, Wallace BA, Sansom MSP. HOLE: a program for the analysis of the pore dimensions of ion channel structural models. *J Mol Graph.* 1996;14:354–60.
 49. Chen VB, Arendall WB, Headd JJ, Keedy D a, Immormino RM, Kapral GJ, et al. MolProbity: all-atom structure validation for macromolecular crystallography. *Acta Crystallogr Sect D Biol Crystallogr.* 2010;66:12–21.
 50. Pronker MF, Bos TG, Sharp TH, Thies-Weesie DM, Janssen BJ. Olfactomedin-1 has a V-shaped disulfide-linked tetrameric structure; 2015. <https://doi.org/10.1074/jbc.M115.653485>.
 51. Harding MM. Small revisions to predicted distances around metal sites in proteins. *Acta Crystallogr Sect D Biol Crystallogr.* 2006;62:678–82.

52. Harding MM. The geometry of metal-ligand interactions relevant to proteins. II. Angles at the metal atom, additional weak metal-donor interactions. *Acta Crystallogr Sect D Biol Crystallogr*. 2000;56:857–67.
53. Glaser F, Pupko T, Paz I, Bell RE, Bechor-Shental D, Martz E, et al. ConSurf: identification of functional regions in proteins by surface-mapping of phylogenetic information. *Bioinformatics*. 2003;19:163–4.
54. Rusakov DA, Fine A. Extracellular Ca²⁺ depletion contributes to fast activity-dependent modulation of synaptic transmission in the brain. *Neuron*. 2003;37:287–97 <http://www.ncbi.nlm.nih.gov/pubmed/12546823>.
55. Araç D, Boucard AA, Özkan E, Strop P, Newell E, Südhof TC, et al. Structures of neuroligin-1 and the neuroligin-1/neurexin-1 β complex reveal specific protein-protein and protein-Ca²⁺ interactions. *Neuron*. 2007;56:992–1003.
56. Fabrichny IP, Leone P, Sulzenbacher G, Comoletti D, Miller MT, Taylor P, et al. Structural analysis of the synaptic protein neuroligin and its β -neurexin complex: determinants for folding and cell adhesion. *Neuron*. 2007;56:979–91.
57. Ko J, Fuccillo MV, Malenka RC, Südhof TC. LRRTM2 functions as a neurexin ligand in promoting excitatory synapse formation. *Neuron*. 2009;64:791–8.
58. Yamagata A, Goto-Ito S, Sato Y, Shiroshima T, Maeda A, Watanabe M, et al. Structural insights into modulation and selectivity of transsynaptic neurexin-LRRTM interaction. *Nat Commun*. 2018;9:1–11. <https://doi.org/10.1038/s41467-018-06333-8>.
59. Elegheert J, Kakegawa W, Clay JE, Shanks NF, Behiels E, Matsuda K, et al. Structural basis for integration of GluD receptors within synaptic organizer complexes. *Science* (80-). 2016;353:295–300.
60. Shapiro L, Chappuis-Flament S, Gumbiner BM, Murray J, Wong E, Boggon TJ. C-cadherin ectodomain structure and implications for cell adhesion mechanisms. *Science* (80-). 2002;296:1308–13.
61. Tai CY, Kim SA, Schuman EM. Cadherins and synaptic plasticity. *Curr Opin Cell Biol*. 2008;20:567–75.
62. Matsuda K, Miura E, Miyazaki T, Kakegawa W, Emi K, Narumi S, et al. Cbln1 is a ligand for an orphan glutamate receptor delta2, a bidirectional synapse organizer. *Science*. 2010;328:363–8. <https://doi.org/10.1126/science.1185152>.
63. Uemura T, Lee S, Yasumura M, Takeuchi T, Yoshida T, Ra M, et al. Trans-synaptic interaction of GluRdelta2 and neurexin through Cbln1 mediates synapse formation in the cerebellum. *Cell*. 2010;141:1068–79. <https://doi.org/10.1016/j.cell.2010.04.035>.
64. Tang A, Chen H, Li TP, Metzbowler SR, MacGillavry HD, Blanpied TA. A trans-synaptic nanocolumn aligns neurotransmitter release to receptors. *Nature*. 2016;536:210–4. <https://doi.org/10.1038/nature19058>.
65. Fanutza T, del Prete D, Ford MJ, Castillo PE, D'Adamio L. APP and APLP2 interact with the synaptic release machinery and facilitate transmitter release at hippocampal synapses. *Elife*. 2015;4:1–27.
66. Laßek M, Weingarten J, Einsfelder U, Brendel P, Müller U, Volkhardt W. Amyloid precursor proteins are constituents of the presynaptic active zone. *J Neurochem*. 2013;127:48–56.
67. Kitov PI, Bundle DR. On the nature of the multivalency effect : a thermodynamic model. *J Am Chem Soc*. 2003;125:16271–84.
68. De Strooper B, Karran E. The cellular phase of Alzheimer's disease. *Cell*. 2016;164:603–15. <https://doi.org/10.1016/j.cell.2015.12.056>.
69. Müller UC, Zheng H. Physiological functions of APP family proteins. *Cold Spring Harb Perspect Med*. 2012;2:1–18.
70. Almeida CG, Tampellini D, Takahashi RH, Greengard P, Lin MT, Snyder EM, et al. Beta-amyloid accumulation in APP mutant neurons reduces PSD-95 and GluR1 in synapses. *Neurobiol Dis*. 2005;20:187–98.
71. Hsieh H, Boehm J, Sato C, Iwatsubo T, Tomita T, Sisodia S, et al. AMPAR removal underlies A β -induced synaptic depression and dendritic spine loss. *Neuron*. 2006;52:831–43.
72. Palop JJ, Chin J, Roberson ED, Wang J, Thwin MT, Bien-Ly N, et al. Aberrant excitatory neuronal activity and compensatory remodeling of inhibitory hippocampal circuits in mouse models of Alzheimer's disease. *Neuron*. 2007;55:697–711.

Publisher's Note

Springer Nature remains neutral with regard to jurisdictional claims in published maps and institutional affiliations.

Ready to submit your research? Choose BMC and benefit from:

- fast, convenient online submission
- thorough peer review by experienced researchers in your field
- rapid publication on acceptance
- support for research data, including large and complex data types
- gold Open Access which fosters wider collaboration and increased citations
- maximum visibility for your research: over 100M website views per year

At BMC, research is always in progress.

Learn more biomedcentral.com/submissions

